AIAA JOURNAL
Vol. 31, No. 8, August 1993

Vorticity Dynamics of Inviscid Shear Layers

Jeffrey W. Yokota*
Sverdrup Technology, Inc., Brook Park, Ohio 44142

The inviscid evolution of a two-dimensional shear layer is simulated numerically by a scheme based on a kinematic decomposition of the unsteady flow. Lagrangian and Weber transformations of the incompressible Euler equations result in a Clebsch representation that separates the flowfield into rotational and irrotational components. These transformations produce the initial construction of the flowfield and define its subsequent evolution.

Introduction

As numerical schemes become more accurate and efficient, computational simulations are being used to investigate flow phenomena of increasing complexity. Analytical methods, although both powerful and informative, are often difficult to apply to nonlinear problems on complex geometries. Numerical techniques, however, allow for the modeling of both geometric and nonlinear complexities. Unfortunately, numerical consistency exists only within the limit of infinitesimally small time steps and grid spacings, where the likelihood of having resources large enough to accomplish such calculations remains remote. Thus practical difficulties occur when trying to extract physically meaningful results from simulations of only medium fineness and accuracy. Consequently, one hopes to improve the performance of more moderately accurate schemes (typically second- or third-order accurate) by incorporating problem-specific flow physics into the numerical solution procedure.

Most currently used inviscid schemes are based on the one-dimensional Euler equations and have unquestionably good shock-capturing capabilities. Unfortunately, their ability to resolve unsteady vortical flows is not yet of equal stature. First, the concept of vorticity does not exist in one dimension, and second, correct wave propagation, a major requirement of any unsteady simulation, is not easily satisfied in multidimensions.

Central-differenced schemes gather information from all directions and are often the methods of choice for elliptic flow calculations. Their use in hyperbolic calculations, however, requires an explicitly added artificial dissipation that, unless tailored judiciously, can significantly reduce spatial accuracy.

Upwind-differenced schemes produce superior one-dimensional results since the flowfield can be resolved along grid directions coincident with the physically upwind ones. Unfortunately, extending these concepts to multidimensions is made difficult by the infinite number of directions and waves from which one must choose to upwind. In the present work, the incompressible Euler equations are decomposed into scalar elliptic and hyperbolic equations to take advantage of the benefits of both central- and upwind-differenced numerical techniques.

Historically, the value of a velocity decomposition scheme could be found in its ability to add rotational effects to steady potential flow calculations.[1-4] However, the use of velocity decomposition schemes became less common as shock capturing became more refined. With the exception of helicopter wake/rotor interactions,[5,6] where the need to conserve vorticity often outweighs any desire to calculate strong shocks, most inviscid compressible flows are currently simulated with shock-capturing schemes. However, despite being restricted to flows with weak shocks, calculations of unsteady vortical flows, such as those associated with fluid mixing, should benefit from a velocity decomposition approach.

An obvious decomposition is the one that splits the flow into rotational and irrotational components.[7,8] Initially this decomposition seems appealing since one hopes to have split the flow into acoustic and vortical fields. Unfortunately, this splitting is not unique since the rotational component can be constructed from the sum of the vortical field and any arbitrary irrotational field (provided this irrotational field is also subtracted from the acoustic component). Thus one cannot assume to have split the flowfield into acoustic and vortical components exclusively.[9] The flow equations are, however, decomposed into scalar elliptic and hyperbolic ones, thereby isolating the vortical field within the rotational component that can then be convected by an appropriate upwind scheme.

Thus the hope of this work is to produce a set of kinematically decomposed flow equations, suited for the simulation of unsteady vortical flows, and solved by appropriate central- and upwind-differenced numerical schemes. To test this approach, a steady shear flow is constructed analytically, reproduced numerically, and then perturbed by an unsteady inflow boundary condition. The inviscid evolution of these inflow disturbances is then simulated from small amplitude wave to nonlinear roll-up. The irrotational component of the flow is constructed from the velocity potential solution of a central-differenced continuity equation. This equation is solved by an approximate lower-upper (LU) factorization scheme that is written within the framework of the multigrid method. The rotational component of the flow is represented by a series of complex-lamellar fields whose components are convected by an upwind-differenced material derivative. The nonlinear interaction between these components is captured by coupling the rotational and irrotational fields during each time step of the unsteady calculation.

Analysis

The incompressible Euler equations can be written in the Cartesian coordinate system (x, y) as

$$\frac{\partial u_i}{\partial x_i} = 0 \tag{1}$$

$$\frac{Du_i}{Dt} = -\frac{1}{\rho}\frac{\partial p}{\partial x_i} \tag{2}$$

Received Nov. 4, 1991; presented as Paper 92-0420 at the AIAA 30th Aerospace Sciences Meeting, Reno, NV, Jan. 6-9, 1992; revision received Jan. 25, 1993; accepted for publication Jan. 29, 1993.

*Senior Research Engineer, NASA Lewis Research Center Group. Member AIAA.

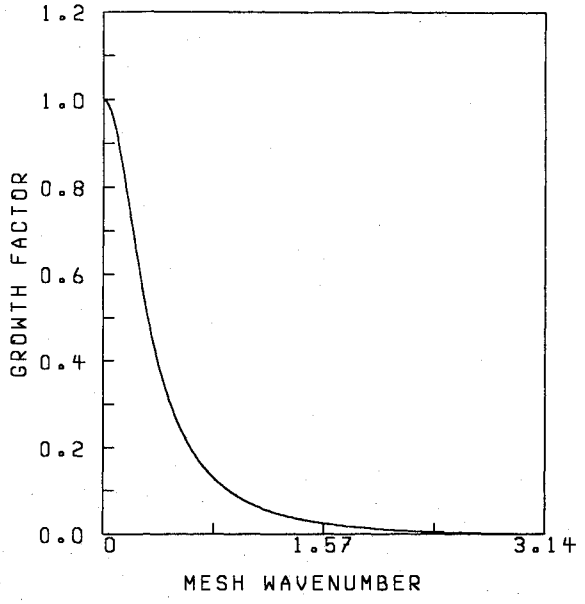

Fig. 1 Growth factor of the LU scheme.

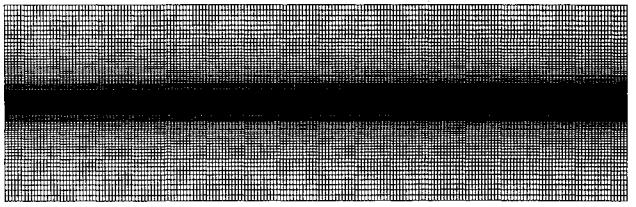

Fig. 2 192 × 96 grid.

Historically, the value of a velocity decomposition scheme could be found in its ability to add rotational effects to steady potential flow calculations.[1-4] However, the use of velocity decomposition schemes became less common as shock capturing became more refined. With the exception of helicopter wake/rotor interactions,[5,6] where the need to conserve vorticity often outweighs any desire to calculate strong shocks, most inviscid compressible flows are currently simulated with shock-capturing schemes. However, despite being restricted to flows with weak shocks, calculations of unsteady vortical flows, such as those associated with fluid mixing, should benefit from a velocity decomposition approach.

An obvious decomposition is the one that splits the flow into rotational and irrotational components.[7,8] Initially this decomposition seems appealing since one hopes to have split the flow into acoustic and vortical fields. Unfortunately, this splitting is not unique since the rotational component can be constructed from the sum of the vortical field and any arbitrary irrotational field (provided this irrotational field is also subtracted from the acoustic component). Thus one cannot assume to have split the flowfield into acoustic and vortical components exclusively.[9] The flow equations are, however, decomposed into scalar elliptic and hyperbolic ones, thereby isolating the vortical field within the rotational component that can then be convected by an appropriate upwind scheme.

Thus the hope of this work is to produce a set of kinematically decomposed flow equations, suited for the simulation of unsteady vortical flows, and solved by appropriate central- and upwind-differenced numerical schemes. To test this approach, a steady shear flow is constructed analytically, reproduced numerically, and then perturbed by an unsteady inflow boundary condition. The inviscid evolution of these inflow disturbances is then simulated from small amplitude wave to nonlinear roll-up. The irrotational component of the flow is constructed from the velocity potential solution of a central-differenced continuity equation. This equation is solved by an approximate lower-upper (LU) factorization scheme that is written within the framework of the multigrid method. The rotational component of the flow is represented by a series of complex-lamellar fields whose components are convected by an upwind-differenced material derivative. The nonlinear interaction between these components is captured by coupling the rotational and irrotational fields during each time step of the unsteady calculation.

Analysis

The incompressible Euler equations can be written in the Cartesian coordinate system (x, y) as

$$\frac{\partial u_i}{\partial x_i} = 0 \tag{1}$$

$$\frac{\mathrm{D}u_i}{\mathrm{D}t} = -\frac{1}{\rho}\frac{\partial p}{\partial x_i} \tag{2}$$

where (u, v) are the Cartesian velocity components, ρ is density, p is pressure, and the material derivative is defined as

$$\frac{\mathrm{D}}{\mathrm{D}t} = \frac{\partial}{\partial t} + u_j\frac{\partial}{\partial x_j} \tag{3}$$

Lagrangian coordinates (X, Y) satisfy

$$\frac{\mathrm{D}X_i}{\mathrm{D}t} = 0 \tag{4}$$

where the Cartesian/Lagrangian transformation matrix is defined as

$$J = \frac{\partial x_i}{\partial X_j} \tag{5}$$

Linear momentum, Eq. (2), is multiplied by the matrix J to produce the following tensor equation:

$$\frac{\mathrm{D}}{\mathrm{D}t}\left(u_i\frac{\partial x_i}{\partial X_j}\right) = \frac{\partial}{\partial X_j}\left(\frac{u_i u_i}{2}\right) - \frac{1}{\rho}\frac{\partial p}{\partial X_j} \tag{6}$$

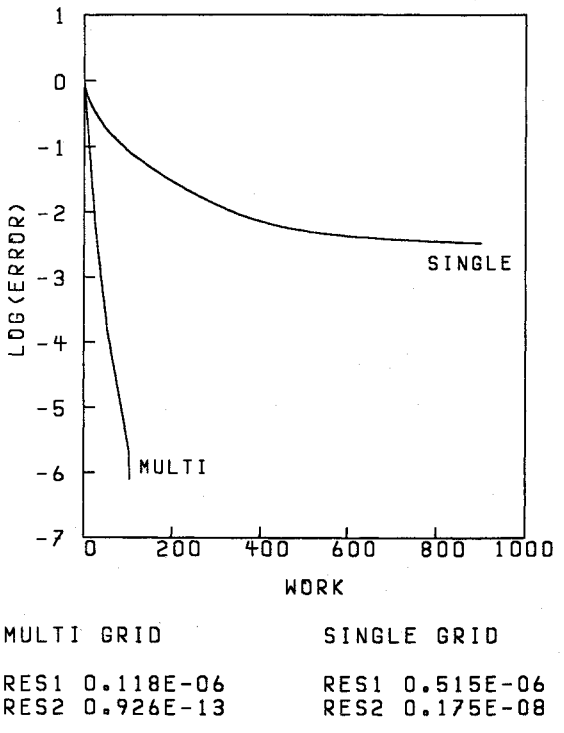

Fig. 3 Convergence history of the LU scheme at $t = 0.01$ ms.

which can then be integrated as follows:

$$\int \frac{D}{Dt}\left(u_i \frac{\partial x_i}{\partial X_j}\right) dt = \int \frac{\partial}{\partial X_j}\left(\frac{u_i u_i}{2} - \frac{p}{\rho}\right) dt \tag{7}$$

such that

$$u_i \frac{\partial x_i}{\partial X_j} - a_j = \frac{\partial}{\partial X_j} \int \left(\frac{u_i u_i}{2} - \frac{p}{\rho}\right) dt \tag{8}$$

where a_j is a constant of integration dependent on the material coordinates (X, Y). If one defines the Weber transformation,[10,11]

$$\frac{D\phi}{Dt} = \frac{u_i u_i}{2} - \frac{p}{\rho} \tag{9}$$

Eq. (8) can then be written as

$$u_i \frac{\partial x_i}{\partial X_j} - A_j + \frac{\partial \phi}{\partial X_j} \tag{10}$$

where A_j is a constant of integration and

$$\frac{DA_j}{Dt} = 0 \tag{11}$$

Equation (10) can now be multiplied by the inverse of matrix J to produce the Clebsch decomposition:

$$u_i = A_j \frac{\partial X_j}{\partial x_i} + \frac{\partial \phi}{\partial x_i} \tag{12}$$

The rotational velocity field at $t = t_0$ is defined as

$$u_i^{r0} = \left(u_i - \frac{\partial \phi}{\partial x_i}\right)\Big|_{t=t_0} \tag{13}$$

and if one sets $X_i = x_i$ at $t = t_0$, then $u_j^{r0} = A_j$ and Eqs. (11) and (12) become

$$\frac{Du_j^{r0}}{Dt} = 0 \tag{14}$$

and

$$u_i = u_j^{r0} \frac{\partial X_j}{\partial x_i} + \frac{\partial \phi}{\partial x_i} \tag{15}$$

An unsteady, incompressible, inviscid vortical flow can now be described by the scalar convection equations, Eqs. (4) and (14), continuity, Eq. (1), and the Clebsch decomposition, Eq. (15), provided the initial condition $X_i = x_i$ is specified at $t = t_0$.

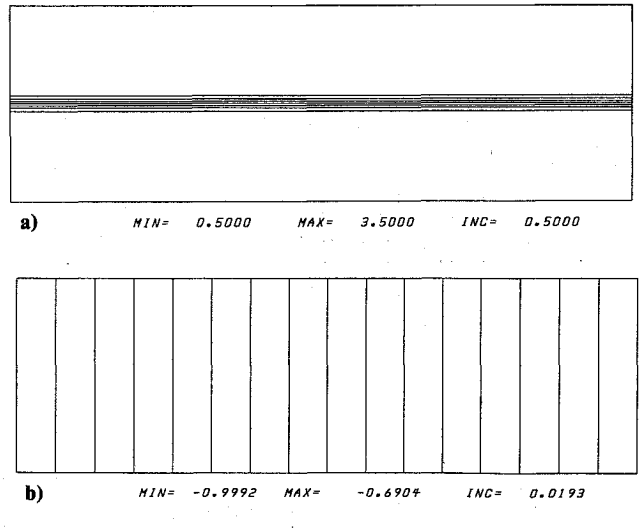

Fig. 4 Initial conditions: a) u^{r0} material field and b) X material field.

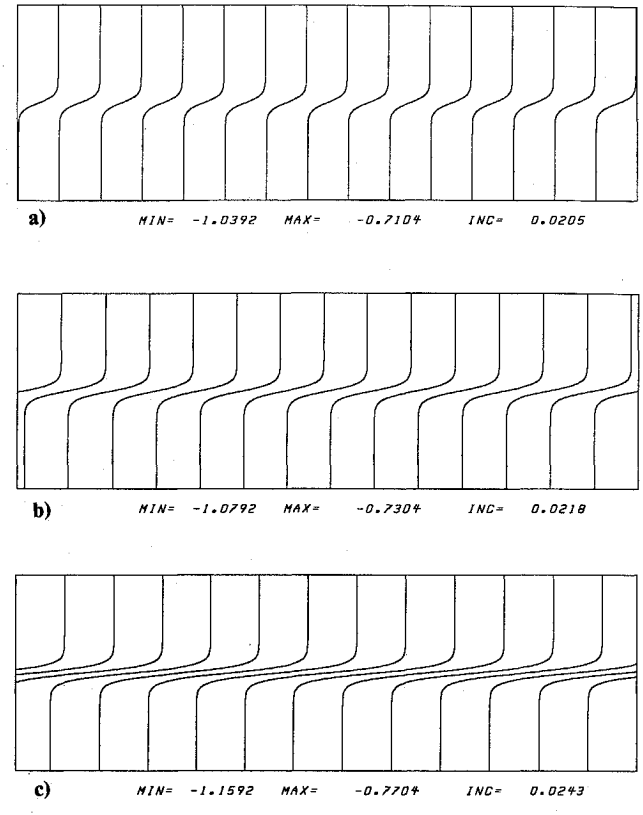

Fig. 5 X material field, steady shear layer: a) $t = 5.0$ ms; b) $t = 10.0$ ms; and c) $t = 20.0$ ms.

Numerical Implementation

The inviscid evolution of an unsteady vortical flow can be simulated with the governing equations described earlier. First the initial flow is analytically decomposed into rotational and irrotational components. The rotational components are then assigned the role of initial conditions for the u_i^{r0} material field, whereas the X_i material lines are equated to the Cartesian coordinates. Finally, a numerical potential field is constructed to ensure that the continuity equation's numerical approximation is not violated within the initial conditions. Once these initial conditions are constructed, the flow simulation evolves by time advancing the convection equations, enforcing continuity, and reconstructing the velocity field within each time step.

Unsteady Convection Scheme

Convection equations (4) and (14) can be written as the decoupled scalar system:

$$\frac{\partial W}{\partial t} + \frac{\partial F}{\partial x} + \frac{\partial G}{\partial y} = 0 \tag{16}$$

This equation is time advanced by a cell-centered finite volume scheme that constructs a piecewise linear distribution over each of the finite volumes, characteristically convects information to an intermediate time level, and updates the cell-centered variables with a midpoint rule time integration.

To ensure the production of a nonoscillatory solution, at least directionally, the piecewise linear distribution is constructed in a nonoscillatory manner. To avoid excessive amounts of damping, this distribution must be at least uniformly second-order accurate. A one-dimensional interpolation can be written as

$$W = W_i + S_i^x (x - x_i) \tag{17}$$

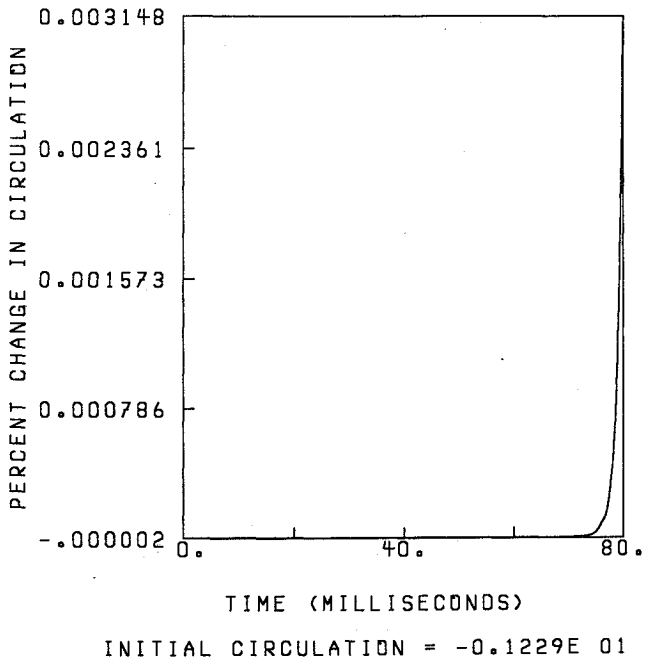

Fig. 6 Circulation history, steady shear layer.

where S_i^x is the slope over each finite volume. The slope associated with Harten and Osher's uniformly second-order accurate UNO2 scheme[12] is written as

$$S_i^x = \frac{\text{median}(0,\ W^c_{i+\frac{1}{2}} - W_i,\ W_i - W^c_{i-\frac{1}{2}})}{\Delta x/2} \tag{18}$$

where $W^c_{i+\frac{1}{2}}$ is obtained from a nonoscillatory quadratic interpolation:

$$W^c_{i+\frac{1}{2}} = 0.5(W_i + W_{i+1}) - 0.25D_{i+\frac{1}{2}} \tag{19}$$

where

$$D_{i+\frac{1}{2}} = \text{minmod}(D_i,\ D_{i+1}) \tag{20}$$

$$D_i = W_{i+1} - 2W_i + W_{i-1}$$

and

$$\text{minmod}(a,\ b) = \text{sign}(a)\max[0,\ \text{sign}(ab)\min(|a|,\ |b|)] \tag{21}$$

Surface data are evaluated at time level $n + \frac{1}{2}$ by following characteristics back to their spatial locations at time level n. For positive convection speeds the surface data at time level $n + \frac{1}{2}$ are written as

$$W^{n+\frac{1}{2}}_{i+\frac{1}{2},j} = W^n_{i,j} + S^x_{i,j}\frac{\Delta x}{2}\left(1 - \frac{u_{i+\frac{1}{2},j}\Delta t}{\Delta x}\right) - S^y_{i,j}\frac{v_{i+\frac{1}{2},j}\Delta t}{2} \tag{22}$$

Once the surface data and their fluxes are constructed at the time level $n + \frac{1}{2}$, the cell-centered values are updated by the midpoint rule:

$$W^{n+1}_{i,j} = W^n_{i,j} - \Delta t\left(\frac{F^{n+\frac{1}{2}}_{i+\frac{1}{2},j} - F^{n+\frac{1}{2}}_{i-\frac{1}{2},j}}{\Delta x} + \frac{G^{n+\frac{1}{2}}_{i,j+\frac{1}{2}} - G^{n+\frac{1}{2}}_{i,j-\frac{1}{2}}}{\Delta y}\right) \tag{23}$$

where $F = Wu$ and $G = Wv$.

Potential Solution Scheme

The continuity equation

$$\nabla \cdot v = \frac{\partial}{\partial x_i}\left(u_j^{r0}\frac{\partial X_j}{\partial x_i} + \frac{\partial \phi}{\partial x_i}\right) = 0 \tag{24}$$

must be satisfied at each time step and produces the velocity potential ϕ. This equation is solved by the approximately LU factored scheme:

$$[1 - \mu\alpha(\delta_x^+ + \delta_y^+)]\cdot[1 + \mu\alpha(\delta_x^- + \delta_y^-)]\Delta\phi_{ij} = \alpha\omega(\delta_x u + \delta_y v)_{ij} \tag{25}$$

where $\Delta\phi_{ij} = \tilde{\phi}_{ij} - \phi_{ij}$; μ and α are scalar constants of $\mathcal{O}(1)$; ω is a relaxation parameter; and δ^+, δ^-, and δ are forward-, backward-, and central-differenced operators, respectively. The residual, Eq. (24), is approximated by a finite volume formulation that constructs fluxes on the faces of each mesh cell. The scalar system is then solved by two explicit sweeps through the domain, similar to the procedures developed for two factored implicit time-marching schemes.[13,14] Within each time step, the maximum residual is reduced to an order of $0(10^{-11})$ before time advancing the flow simulation.

To illustrate the potential convergence properties of this scheme, a von Neumann stability analysis is performed on the one-dimensional equation:

$$\frac{\delta^2\phi}{\delta x^2} = 0 \qquad \text{where} \qquad \phi_j^n = G^n e^{i\beta x_j}$$

The approximate LU factored scheme

$$(1 - \mu\alpha\delta_x^+)\cdot(1 + \mu\alpha\delta_x^-)\Delta\phi_j = \alpha\omega\delta_{xx}\phi_j$$

has the growth factor

$$G = \frac{1 - 4\alpha[\omega - \mu(1 + \mu\alpha)]\sin^2(\beta\Delta x/2)}{1 + 4\mu\alpha(1 + \mu\alpha)\sin^2(\beta\Delta x/2)}$$

and is plotted in Fig. 1 for $\mu = 0.5$, $\alpha = 5.3$, and $\omega = 1.9$. The growth factor has a strong high wave number damping that makes this scheme receptive to multigrid acceleration. Thus the approximate LU scheme is written within the framework of the multigrid method to accelerate these calculations to a steady state. During each time step of the unsteady simulation, a six multigrid level W cycle is used to accelerate the LU scheme to convergence.

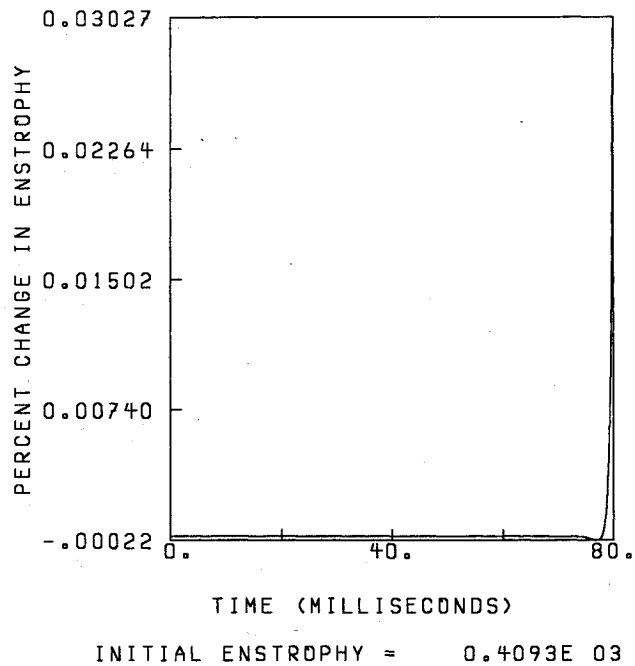

Fig. 7 Enstrophy history, steady shear layer.

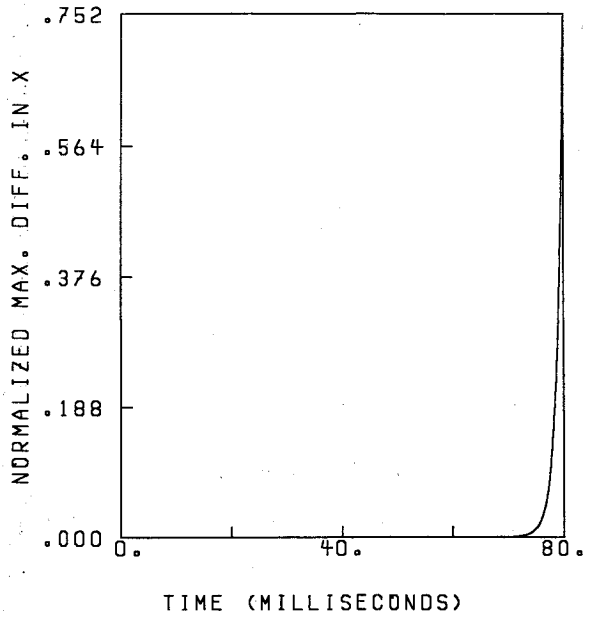

Fig. 8 Error history of the X material field, steady shear layer.

Analytical Steady Flow

A steady, quasi-two-dimensional shear layer can be modeled[15]:

$$u = \bar{u}(1 + R \tanh \beta) \tag{26}$$

$$v = 0 \tag{27}$$

where $\beta = 0.5(y - y_c)/\theta$, $\bar{u} = 0.5(u_1 + u_2)$, $\Delta u = u_2 - u_1$, $R = 0.5\,\Delta u/\bar{u}$, θ is the momentum thickness, y_c is the centerline, and u_1 and u_2 are the velocities of the two coflowing streams. A Clebsch decomposition that satisfies Eqs. (1), (4), (14), (15), (26), and (27) can be written as

$$u^{r0} = \bar{u}(1 + R \tanh \beta) - u_1 \tag{28}$$

$$v^{r0} = 0 \tag{29}$$

$$X = x - \bar{u}t(1 + R \tanh \beta) \tag{30}$$

$$Y = y \tag{31}$$

$$\phi = u_1 x + \frac{\bar{u}Rt}{2} \tanh \beta(\Delta u + \bar{u}R \tanh \beta) \tag{32}$$

This decomposition will be used to construct the initial conditions for the shear layer simulations to follow. Vortical phenomena such as vortex sheet/shear layer roll-up have, traditionally, been best simulated by vortex methods based on the evolution of point vortices, vortex blobs, or vortex patches. Point vortex methods were initially quite successful in simulating the roll-up of vortex sheets[16,17] until it was observed that the velocity field became singular as the distance between the vortices was reduced.[18] This difficulty was later overcome by the introduction of the vortex blob method.[19,20] Schemes based on contour dynamics, or the evolution of vortex patches, have also been impressive in their simulation of two-dimensional inviscid flow.[21,22]

The present work attempts to emulate the success of these methods by recognizing the need to tailor one's numerical approach around the convection of vorticity without having to reconstruct the velocity field from the unsteady vorticity field.

Numerical Aspects

Shear layer calculations, characterized by $u_1 = 4.0$ m/s, $u_2 = 8.0$ m/s, and $\theta = 2.0$ mm, are performed on a 192×96 grid (Fig. 2). This grid has a uniform streamwise spacing of 1.6 mm and is algebraically stretched in the cross-stream direction. The cross-stream distribution has approximately 30 cells within the initial shear layer, 10 of which are within the momentum thickness. The smallest cell is 0.2 mm thick and located at the centerline, whereas the computational domain is approximately 0.1 m wide and 0.3 m long.

Equation (30) suggests that infinite stretching and shearing of the X material lines are produced as $t \to \infty$. Thus calculations of a long duration are limited in value, since physical viscosity normally acts to dampen this shearing. Furthermore, at the centerline of the shear layer ($\beta = 0$), the gradient $\partial X/\partial y \to \infty$ as $t \to \infty$ and thus Eq. (27)

$$v = \frac{\partial \phi}{\partial y} + u^{r0}\frac{\partial X}{\partial y} = 0$$

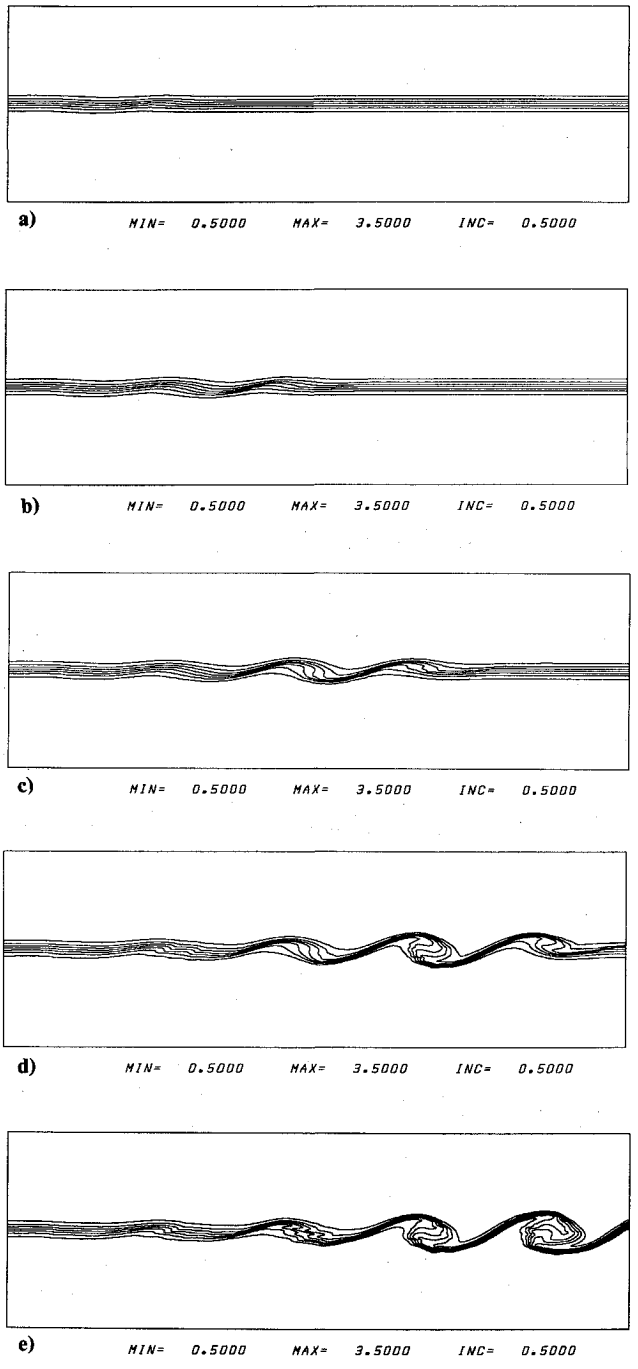

Fig. 9 Forced shear layer, u^{r0} material field: a) $t = 15.0$ ms; b) $t = 25.0$ ms; c) $t = 35.0$ ms; d) $t = 45.0$ ms; and e) $t = 55.0$ ms.

becomes increasingly difficult to satisfy numerically. Since the gradient of X is not bounded in time, neither are the truncation errors of its numerical approximation. Thus cross-stream velocity disturbances, capable of triggering the shear instability, are likely to be generated at the centerline. On the grid described earlier, these disturbances become noticeable after 70 ms or 7000 time steps. Unless the Lagrangian coordinates are periodically reinitialized, these simulations must be limited to a duration of 70 ms. Despite these limitations, the short-term dynamics of rapidly growing initial disturbances can be simulated by these inviscid equations.

The steady flow is reproduced numerically to evaluate the scheme's fidelity. Even though the flow is steady, the X material lines' time-dependent behavior can be used to evaluate the scheme's performance. The initial conditions are constructed analytically at $t = 0$, and the velocity potential is recast as a perturbation on a uniform flow. Thus

$$\phi = u_1 x + \tilde{\phi} \tag{33}$$

An inviscid no-flux or parallel flow condition

$$\frac{\partial u^{r0}}{\partial y} = \frac{\partial \tilde{\phi}}{\partial y} + u^{r0}\frac{\partial X}{\partial y} = 0 \tag{34}$$

is specified at both the top and bottom boundaries of the domain, whereas the outflow condition

$$\frac{\partial^2 u^{r0}}{\partial x^2} = \frac{\partial^2 X}{\partial x^2} = \frac{\partial^2 \tilde{\phi}}{\partial y^2} + \frac{\partial}{\partial y}\left(u^{r0}\frac{\partial X}{\partial y}\right) = 0 \tag{35}$$

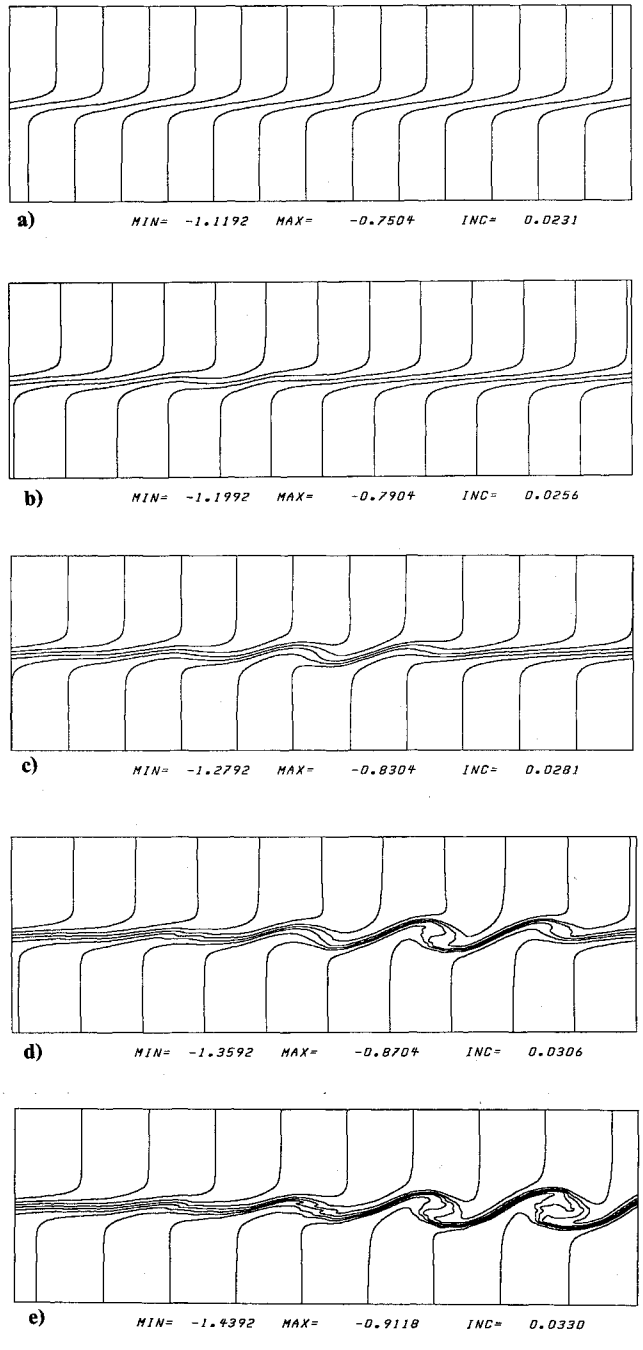

Fig. 10 X **material field, forced shear layer: a)** $t = 15.0$ **ms; b)** $t = 25.0$ **ms; c)** $t = 35.0$ **ms; d)** $t = 45.0$ **ms; and e)** $t = 55.0$ **ms.**

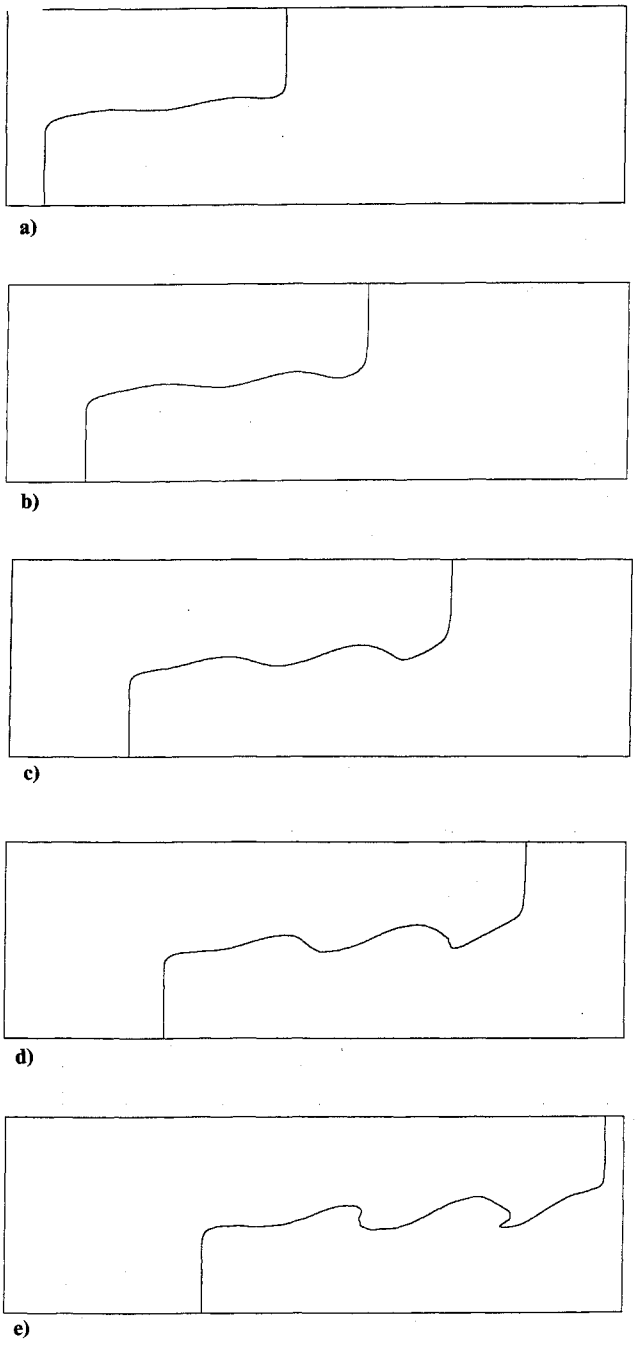

Fig. 11 $X = -1.10$ **material line, forced shear layer: a)** $t = 30.0$ **ms; b)** $t = 35.0$ **ms; c)** $t = 40.0$ **ms; d)** $t = 45.0$ **ms; and e)** $t = 50.0$ **ms.**

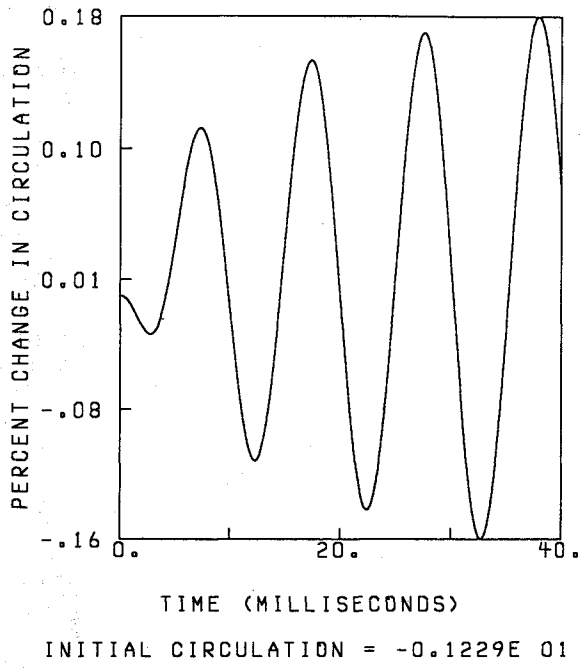

Fig. 12 Circulation history, forced shear layer.

and

$$\tilde{\phi}(x_l, y_h) = 0 \tag{36}$$

is specified at $x = x_l$. A steady inflow condition

$$u^{r0} = \bar{u}(1 + R \tanh \beta) - u_1$$

$$v^{r0} = \frac{\partial \tilde{\phi}}{\partial x} = 0 \tag{37}$$

$$\frac{\partial X}{\partial x} = 1$$

is specified at $x = x_0$.

Once the scheme's fidelity is verified, the roll-up of the shear layer is accelerated by oscillating inflow disturbances. The inflow boundary condition, Eq. (37), is modified with an oscillating centerline:

$$\beta = \frac{(y - \tilde{y}_c)}{2\theta}$$

$$\tilde{y}_c = y_c + K\theta \sin(\omega t) \tag{38}$$

$$\omega = \frac{2\pi S_n \bar{u}}{\theta}$$

where $S_n = 0.032$ is the Strouhal number associated with the shear layer's natural frequency,[15] and K is a scalar constant. The initial roll-up of the shear layer results from the inviscid shear flow instability[23] and should be simulated accurately. Subsequent development may not evolve correctly since vortices grow through the continuous ingestion of irrotational fluid, and vortex pairing can occur at saturation.[24] However, a kinematic description assumes a continuous mapping of the material lines that can undergo stretching and folding but not breakage and amalgamation. Consequently, an inviscid simulation of these growing disturbances is most valid during their initial amplification. Despite these limitations, results from a kinematic-based scheme should contribute to the understanding of fluid mixing because from a kinematical viewpoint fluid mixing is the efficient stretching and folding of material lines and surfaces.[25]

Furthermore, the tagging of homogenous subsonic flows, both experimentally and numerically, is often made difficult by the rapid diffusion of the marker species. Thus coherent structures are often visualized through schlieren photographs of stratified flows.[26] Consequently, a kinematic-based scheme, capable of quantitative rather than simply qualitative flow visualization, would be valuable.

Results

The first test case is a numerical reproduction of the analytical steady flow. A constant time step size of 0.01 ms is used in this calculation. Since this steady flow simulation is both two dimensional and inviscid, the following collection of first integrals,

$$I_n = \int_\sigma \omega^n \, da \qquad n = 1, 2, \ldots, \infty \tag{39}$$

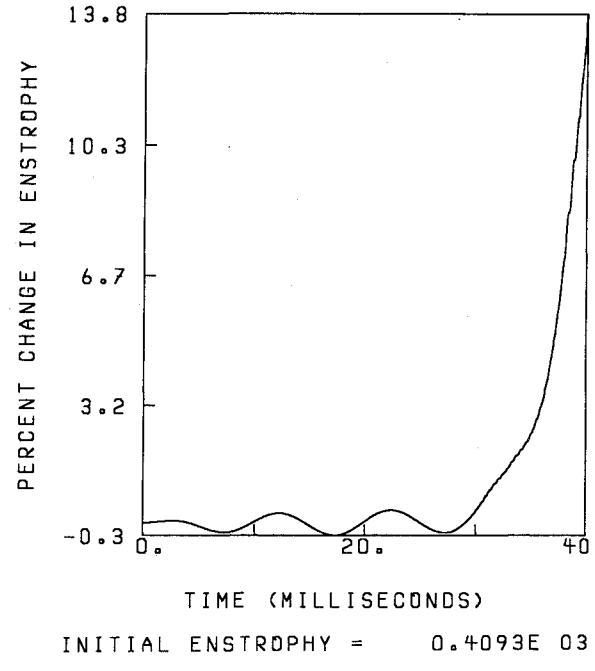

Fig. 13 Enstrophy history, forced shear layer.

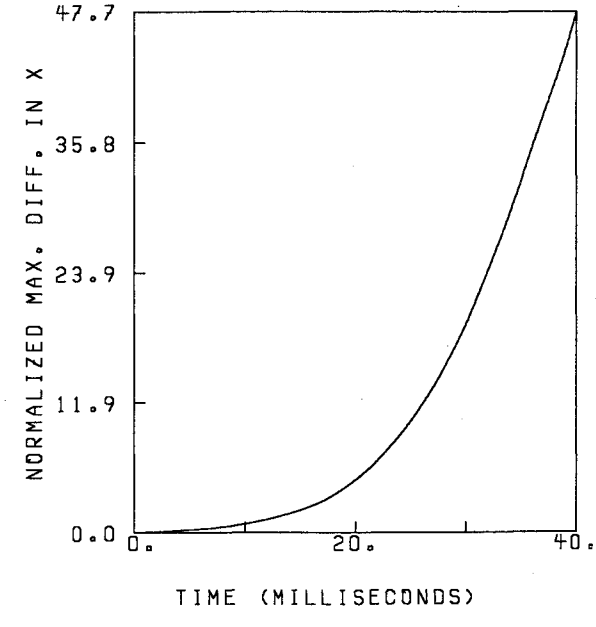

Fig. 14 Error history of the X material field, forced shear layer.

where ω is vorticity, should remain constant over the computational domain. As a measure of the scheme's ability to reproduce this flow, changes in circulation (I_1) and enstrophy (I_2), as well as the maximum absolute error in the X material lines, are monitored. The error in X is calculated with respect to the analytical solution Eq. (30), normalized by θ, and increases as this simulation makes a transition into an unsteady flow.

To illustrate the convergence acceleration produced by the multigrid scheme, both single and multigrid convergence histories of the potential calculation at $t = 0.01$ ms are shown in Fig. 3. A six multigrid level W cycle converged the average residual to $\mathcal{O}(10^{-14})$ in roughly four iterations, each of which is equivalent to approximately 25.7 work units or fine grid calculations.

The initial conditions are assumed to exist for $-\infty < x < +\infty$ but are evaluated only within the finite domain shown in Fig. 4. Although the calculated flow remains steady, the u^{r0} material lines remain identical to the initial condition (Fig. 4a), and the X lines, as predicted from the analytical solution, shear continuously with the flow (Fig. 5).

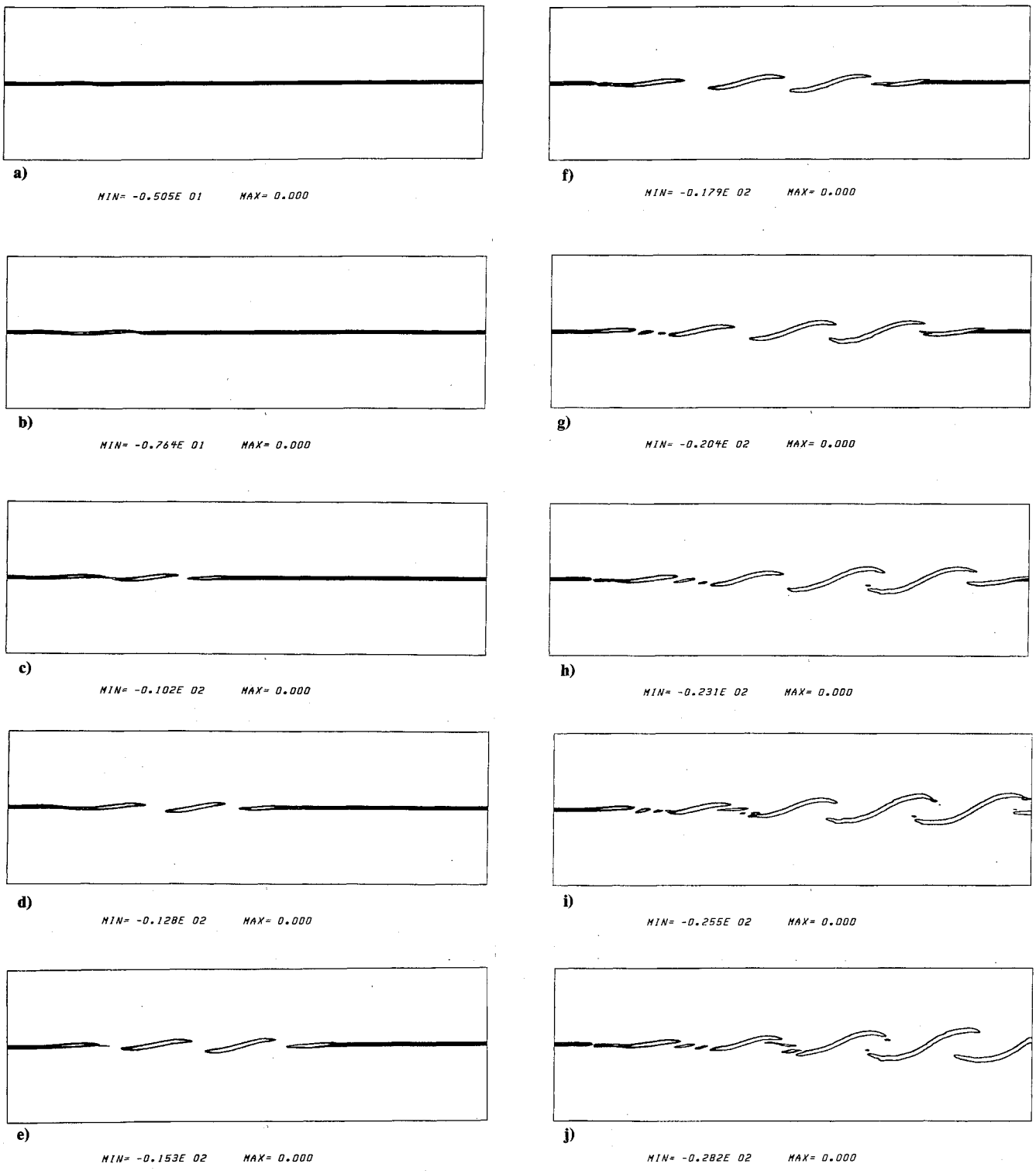

Fig. 15 Cross-stream gradient of the X material field, forced shear layer: a) $t = 10.0$ ms; b) $t = 15.0$ ms; c) $t = 20.0$ ms; d) $t = 25.0$ ms; e) $t = 30.0$ ms; f) $t = 35.0$ ms; g) $t = 40.0$ ms; h) $t = 45.0$ ms; i) $t = 50.0$ ms; and j) $t = 55.0$.

This simulation also tests the inflow/outflow boundary conditions since upstream traveling disturbances, orders of magnitude larger than the interior truncation errors of the discretized equations, are often generated from downstream boundary conditions. This problem is acute for zeroth-order extrapolations but seems not to exist, at least within the time duration of interest, for a first-order treatment. One would expect to see significant variations in circulation and/or exponential growth in enstrophy if the boundary conditions were triggering the shear flow instability. In fact, both circulation (Fig. 6) and enstrophy (Fig. 7) remained essentially constant with only an extremely small error in the X material field (Fig. 8) evident during the first 6000 time steps ($t < 60$ ms). Although this error grows as it is convected, its growth is not exponential and will not reach a size large enough to render the flow unsteady for some time.

In fact, it is only after these first 6000 time steps that one begins to see the excitation of the shear flow instability and the start of its exponential growth. Cross-stream gradients of the X material field increase in magnitude; with this behavior comes an increasing potential to generate centerline disturbances. Any existing initial disturbances do not grow exponentially from $t = 0$, and thus the shear instability is more likely to have been triggered by centerline disturbances generated at $t > 50$ ms. To observe the roll-up of the shear layer within a more timely fashion and without the question of its numerical origin, one must add some physical forcing to the flow. By forcing the flow, the roll-ups can be generated before the material lines have sheared beyond a questionable accuracy.

The second test case is the streamwise development of a forced shear layer. The amplitude of the centerline oscillation is one-tenth the momentum thickness and therefore confined to within the width of the smallest mesh cell. The frequency of this oscillation corresponds to the natural frequency Strouhal number of $S_n = 0.032$ and a constant time step size of 0.01 ms is again used in the time advancement. This inviscid simulation is most valid in regions where the forced disturbances are being amplified and the resulting vortices are becoming fully developed. Conversely, the accuracy of an inviscid approach is less likely to be valid during viscous dominated behavior such as vortex pairing and amalgamation.

Within the shear layer, the discrete contours of the u^{r0} material lines are equivalent to streak lines passing through the inflow boundary. The evolution of these material lines is an important aspect of flow visualization since streak lines can often reveal more information about an unsteady flow than either streamlines or pathlines.[27]

The evolution of the u^{r0} and X material lines is shown in Figs. 9 and 10 where one can see the shear flow instability develop from small amplitude wave to nonlinear roll-up. The linear growth of these small amplitude waves can be seen in both the u^{r0} (Figs. 9a and 9b) and the X (Figs. 10a and 10b) material fields. A distinct steepening of the u^{r0} material lines can be observed in Fig. 9b with their eventual roll-up occurring with subsequent evolution. The leading vortex quickly becomes saturated (Fig. 9d), whereas subsequent vortices continue to grow as they convect downstream. Since this is an inviscid simulation, the internal roll-ups of the material lines are somewhat removed from the more smoothly evolving viscous phenomena. The inviscid shearing of the X material lines produces a temporally increasing cross-stream gradient that, when disturbed, can roll up infinitely. A simple spiraling, however, does not occur because within these vortical roll-ups the material lines are becoming increasingly difficult to resolve. From a numerical perspective, the material lines are not just passively convected by the flow but rather coupled to its construction. Moreover, the accuracy of the computed flowfield is related directly to the resolution of the material fields. Again it is the gross shapes of the initial roll-ups that are most accurately captured inviscidly. Subsequent roll-ups are not produced by the initial instability and are often the result of vortex pairing, and the accuracy of their simulation is more likely to be dominated by viscosity or the lack thereof.

The evolution of an individual X material line is shown in Fig. 11. This line originates outside of the domain and is convected through the inflow boundary condition. The flow is assumed to be steady upstream of the boundary and relative to the oscillating centerline. Within Fig. 11 one can see the material line stretch and fold as it convects downstream through the large vortical structures. Within the time duration shown from Fig. 11a to Fig. 11e, the length of this material line has increased approximately 48%. By comparing these results with the simulation of the analytical steady flow, one can attribute 26% of this stretching to the presence of the vortical roll-ups.

Oscillations generated by the inflow forcing can be seen in the circulation history, Fig. 12, where the magnitude of these growing oscillations is within 0.18%. The enstrophy history consists of an initially linear growth that makes a transition into an exponential one after approximately 30 ms or three cycles of the inflow forcing (Fig. 13). This transition corresponds to the steepening of the small amplitude waves that can be seen in Figs. 9c and 9d. Flow disturbances grow exponentially from $t = 0$ and are reflected in the error history of the X material field, Fig. 14. This error, referenced to the analytical steady solution, grows exponentially from $t = 0$ and, as the shear instability becomes nonlinear, reflects the flow's growing transition to unsteadiness.

The stretching and redistribution of the shear layer are depicted in the evolution of the X material field's cross-stream gradients, Fig. 15. For visual clarity, only the largest 10% of the gradient field is contoured within each of these figures. One can see how the shear layer bends, breaks (Fig. 15c), and ultimately evolves into a number of discrete structures. Once the initial breakage occurs, the shear layer continues to be drawn, pinched, and redistributed into discrete clumps (Figs. 15c–15e). Initially these structures are formed at approximately 10-ms intervals, which corresponds to the period of the inflow forcing. Eventually these structures are stretched and bent into self-similar shapes as they are convected downstream past the vortical roll-ups (Figs. 15f–15j).

Concluding Remarks

A kinematic decomposition of the incompressible Euler equations was derived for the calculation of unsteady vortical flows. Toward this goal, both a uniformly second-order accurate, nonoscillatory convection scheme and an approximately LU factored multigrid scheme were developed for hyperbolic and elliptic, respectively.

To test this approach and verify the scheme's fidelity, a two-dimensional steady shear layer was calculated and compared with its analytical solution. An oscillating inflow was then introduced to accelerate the shear layer's roll-up. The bending and stretching of the material lines as they are convected past the growing vortical disturbances could be seen in these simulations.

The value of this kinematic-based scheme can be found within the quantitative visualization of fluid mixing. Rapidly evolving phenomena can be simulated inviscidly, whereas calculations of long duration or of time periodic flows will require the inclusion of physical viscosity.

Acknowledgments

This work was supported by the NASA Lewis Research Center under Contract NAS3-25266 with John Adamczyk as monitor. It is with pleasure that the author acknowledges a number of helpful conversations with John Adamczyk of NASA Lewis and Kristine Dugas, Edmane Envia, and Ambady Suresh of Sverdrup Technology.

References

[1]Murman, E. M., and Stremel, P. M., "A Vortex Wake Capturing Method for Potential Flow Calculations," AIAA Paper 82-0947, June 1982.

[2]Lacor, C., and Hirsch, C., "Rotational Flow Calculations in Three-Dimensional Blade Passages," American Society of Mechani-

cal Engineers, ASME Paper 82-GT-316, 1982.

[3]Grossman, B., "The Computation of Inviscid Rotational Gasdynamic Flows Using an Alternate Velocity Decomposition," AIAA 6th Computational Fluid Dynamics Conference, AIAA Paper 83-1900, Danvers, MA, July 1983.

[4]Ecer, A., and Akay, H. U., "A Finite Element Formulation for Steady Transonic Euler Equations," *AIAA Journal,* Vol. 21, No. 3, 1983, pp. 343–350.

[5]Steinhoff, J., and Suryanarayana, K., "The Treatment of Vortex Sheets in Compressible Potential Flow," AIAA 6th Computational Fluid Dynamics Conference, AIAA Paper 83-1881, Danvers, MA, July 1983.

[6]Ramachandran, K., Tung, C., and Caradonna, F. X., "The Free-Wake Prediction of Rotor Hover Performance Using a Vortex Embedding Method," AIAA 27th Aerospace Sciences Meeting, AIAA Paper 89-0638, Reno, NV, Jan. 1989.

[7]Hawthorne, W. R., "On the Theory of Shear Flows," Massachusetts Inst. of Technology Gas Turbine Lab., Cambridge, MA, Rept. 88, Oct. 1966.

[8]Chang, S.-C., and Adamczyk, J. J., "A New Approach for Solving the Three-Dimensional Steady Euler Equations. I. General Theory," *Journal of Computational Physics,* Vol. 60, Aug. 1985, pp. 23–40.

[9]Kraichnan, R. H., "The Scattering of Sound in a Turbulent Medium," *Journal of the Acoustical Society of America,* Vol. 25, No. 6, 1953, pp. 1097–1104.

[10]Serrin, J., "Mathematical Principles of Classical Fluid Mechanics," *Encyclopedia of Physics,* edited by S. Flugge, Vol. VIII/1, Springer-Verlag, Berlin, Germany, 1959, pp. 125–263.

[11]Truesdell, C., *The Kinematics of Vorticity,* Indiana Univ. Press, Bloomington, IN, 1954.

[12]Harten, A., and Osher, S., "Uniformly Higher-Order Accurate Nonoscillatory Schemes I," *SIAM Journal of Numerical Analysis,* Vol. 24, April 1987, pp. 279–309.

[13]Anderson, W. K., Thomas, J. L., and Whitfield, D. L., "Multigrid Acceleration of the Flux Split Euler Equations," AIAA 24th Aerospace Sciences Meeting, AIAA Paper 86-274, Reno, NV, Jan. 1986.

[14]Yokota, J. W., and Caughey, D. A., "An LU Implicit Multigrid Algorithm for the Three-Dimensional Euler Equations," *AIAA Journal,* Vol. 26, Sept. 1988, pp. 1061–1069.

[15]Ho, C.-M., and Huerre, P., "Perturbed Free Shear Layers," *Annual Review of Fluid Dynamics,* Vol. 16, 1984, pp. 365–424.

[16]Rosenhead, L., "The Formation of Vortices from a Surface of Discontinuity," *Proceedings of the Royal Society of London Series A,* No. 134, 1931, pp. 170–192.

[17]Westwater, F. L., "Rolling Up of the Surface of Discontinuity Behind an Aerofoil of Finite Span," Aeronautical Research Council, R. and M., Britain, Vol. 1962, 1935.

[18]Birkhoff, G., "Helmoholtz and Taylor Instability," *Proceedings of the 13th Symposium on Applied Mathematics,* XIII, Vol. 55, American Mathematical Society, Providence, RI, 1962, p. 55.

[19]Chorin, A. J., and Bernard, P. S., "Discretization of a Vortex Sheet with an Example of Roll-Up," *Journal of Computational Physics,* Vol. 3, Oct. 1973, pp. 429–433.

[20]Krasny, R., "Desingularization of Periodic Vortex Sheet Roll-Up," *Journal of Computational Physics,* Vol. 65, Aug. 1986, pp. 292–313.

[21]Zabusky, N. J., Hughes, M. H., and Roberts, K. V., "Contour Dynamics for the Euler Equations in Two Dimensions," *Journal of Computational Physics,* Vol. 30, Jan. 1979, pp. 96–106.

[22]Pullin, D. J., and Jacobs, P. A., "Inviscid Evolution of Stretched Vortex Arrays," *Journal of Fluid Mechanics,* Vol. 171, Oct. 1986, pp. 377–406.

[23]Saffman, P. C., "Coherent Structures in Turbulent Flow," *The Role of Coherent Structures in Modelling Turbulence and Mixing,* edited by J. Jimenez, Lecture Notes in Physics, No. 136, Springer-Verlag, New York, 1981, pp. 1–9.

[24]Winant, C. D., and Browand, F. K., "Vortex Pairing: The Mechanism of Turbulent Mixing-Layer Growth at Moderate Reynolds Number," *Journal of Fluid Mechanics,* Vol. 2, No. 63, 1974, pp. 237–255.

[25]Ottino, J. M., *The Kinematics of Mixing: Stretching, Chaos, and Transport,* Cambridge Univ. Press, New York, 1990.

[26]Brown, G. L., and Roshko, A., "On the Density Effects in Turbulent Mixing Layers," *Journal of Fluid Mechanics,* Vol. 4, No. 64, 1974, pp. 775–816.

[27]Hamma, F. R., "Streaklines in a Perturbed Shear Flow," *Physics of Fluids,* Vol. 5, No. 6, 1962, pp. 644–650.